crystals

MDPI

Article

Effect of WO_3 Nanoparticles on the Radiative Attenuation Properties of $SrTiO_3$ Perovskite Ceramic

M. I. Sayyed [1,2,*], S. Hashim [2], E. Hannachi [3], Y. Slimani [4] and M. Elsafi [5]

[1] Department of Physics, Faculty of Science, Isra University, Amman 11622, Jordan
[2] Physics Department, Faculty of Science, Universiti Teknologi Malaysia, Skudai 81310, Johor, Malaysia
[3] Department of Nuclear Medicine Research, Institute for Research and Medical Consultations (IRMC), Imam Abdulrahman Bin Faisal University, P.O. Box 1982, Dammam 31441, Saudi Arabia
[4] Department of Biophysics, Institute for Research and Medical Consultations (IRMC), Imam Abdulrahman Bin Faisal University, P.O. Box 1982, Dammam 31441, Saudi Arabia
[5] Physics Department, Faculty of Science, Alexandria University, Alexandria 21511, Egypt
* Correspondence: dr.mabualssayed@gmail.com

Abstract: In the present work, an experimental study is performed to study the radiation shielding characteristics of $SrTiO_3$ (STO) perovskite ceramic added with different amounts (x = 0, 2, 5, and 10%) of tungsten trioxide nanoparticles (WO_3 NPs). The four ceramic samples were prepared using the solid-state reaction method. The structural properties were examined using X-ray diffraction (XRD) and Fourier transform infrared spectroscopy (FTIR) techniques. The analysis showed the successful formation of WO_3- doped STO samples. The crystallite size, estimated using the Scherrer equation, was found in the range of 50.86–41.17 nm. The effect of WO_3 NPs on the radiation shielding performance of these ceramics was studied. Different parameters, such as linear attenuation coefficient (LAC) and other related factors, were experimentally determined. The linear attenuation coefficient results demonstrated that the additional amount of WO_3 in the ceramics correlates with an improvement in their shielding abilities. The half-value layer (HVL) values for the ceramics with 2% WO_3 nanoparticles are equal to 0.071, 1.760, 2.407, and 2.564 cm at 0.060, 0.662, 1.173, and 1.333 MeV, respectively. As the energy increases, more radiation can pass through the material; therefore, a larger thickness is required to absorb half of the total photons, leading to a greater HVL. The tenth value results reaffirmed that increasing the WO_3 content in the STO ceramics improves their shielding efficiency. The radiation protection efficiency (RPE) of the four prepared STO ceramics was reported. From the RPE, we found that more photons can be attenuated at lower energies.

Keywords: $SrTiO_3$; WO_3 nanoparticles; XRD; FTIR; radiation attenuation

Citation: Sayyed, M.I.; Hashim, S.; Hannachi, E.; Slimani, Y.; Elsafi, M. Effect of WO_3 Nanoparticles on the Radiative Attenuation Properties of $SrTiO_3$ Perovskite Ceramic. *Crystals* **2022**, *12*, 1602. https://doi.org/10.3390/cryst12111602

Academic Editors: Hany Abdo and Ahmed Fouly

Received: 17 October 2022
Accepted: 8 November 2022
Published: 10 November 2022

1. Introduction

The use of radiation has been growing during the past decades in various areas, including agricultural, industrial, and medical fields. Despite the enormous profits of radiation, it has the prospect of causing a significant risk hazard to human safety and the environment. Three basic concepts are followed for better radiation protection: minimizing the exposure time, increasing the distance that separates the entity of question and the source of radiation as much as possible, and using a protective material to isolate the entity of question from radiation. These three concepts are applied as far as practicable to reduce the entire absorbed dose due to radiation exposure [1].

The rendering of a material as a radiation shield is frequently evaluated by its ability to stop the penetration of incident radiation through various mechanisms of interaction. γ radiation, categorized as high penetrating potential, interacts with the material in three distinct processes: Compton scattering (CS), pair production (PP), and photoelectric absorption (PA) [2]. The probability of each interaction occurring is dependent on the incident γ radiation power and the composition of the protective material. PA is the main process

for low energy γ radiation that interacts with materials with high atomic numbers. For high-energy γ radiation, PP became the dominant process. The γ interaction behavior with the shield is characterized by the linear attenuation coefficient (LAC), which depends on the properties of the material, the energy, and the incident radiation. Appropriate shielding material is able to attenuate γ radiation with minimum change to its thermal, mechanical, and physical properties as well as its chemical stability. In general, many factors must be considered when designing a radiation shield, including the kind and intensity of radiation, its energy level, cost, toxicity, and weight of material [3–6].

The frequently employed shielding materials are lead, concrete, and alloys. Studies searching for developed materials for radiation shielding applications have increased owing to their important role in progressed technologies that need ionizing radiations, such as nuclear medicine, radiology, and the characterization of materials. This necessitates advanced materials to be employed in the fabrication of protective structures to shelter humans and the environment from the hurtful impact of ionizing radiation. Aygün et al. studied heavy concretes holding chrome-ore for nuclear radiation shielding applications [7]. Their results showed better shielding properties for concretes with aggregates and additives compared to some heavy concretes and standard concrete [7]. M.I. Sayyed et al. prepared four alloys, including CrTe, $CrTe_{0.95}Sb_{0.05}$, $CrTe_{0.90}Sb_{0.10}$, and $CrTe_{0.8}0Sb_{0.20}$, using a solid-state reaction. The results showed that replacing Te with Sb in the different alloys causes an improvement in their linear attenuation coefficient [8].

Glass-based materials are also common shielding materials and are possible alternatives to concretes for radiation-shielding purposes [9–14]. Glass materials display unique properties that make them useful for some industrial and technical applications. For example, T. H. Khazaalah et al. used soda–lime–silica (SLS) glass waste to fabricate free-Pb glass shielding [8]. γ-ray shielding properties of borate and phosphate glasses containing BaO, Bi_2O_3, and PbO in different ratios were previously studied. The results showed good attenuation properties of these glass systems [10,11]. In addition, the radiation shielding efficiency of borosilicate glass, which consists of silica and boron oxide, has been studied [12]. A recent report showed that borosilicate glass (30 mol%) mixed with 20 mol% of Bi_2O_3 and 50 mol% of BaO displays the highest density value and better radiation shielding performances [14].

Perovskite-based ceramic materials have attracted great interest due to their unique characteristics [15–17]. $SrTiO_3$ (STO) is a model of the perovskite-like ceramic material with many important properties and possible uses in diverse applications such as optoelectronic [18], photovoltaic [19,20], photocatalytic [20,21], and energy storage applications [22]. STO displays a high dielectric constant, average permittivity, and low tangent loss [14]. STO has also proven its efficacity in the domain of radiation shielding [23–25]. Moreover, STO is a mixed conducting perovskite [23,24] which can be influenced by doping and/or addition, temperature, and oxygen partial pressure (pO_2). For instance, E. Hannachi et al. studied the radiation-protecting properties of STO doped with tin oxide. The results showed that tin oxide addition enhanced the radiation shielding capacity of STO ceramic [23].

Metal oxide semiconductors play an interesting role in different areas of science, such as engineering, medicine, physics, chemistry, etc. Metal oxide semiconductors have gained much interest owing to their particular optical, magnetic, and electrical properties. Among the most useful metal oxide semiconductors, WO_3 has been employed for different applications such as electrocatalyst [26], photocatalyst [27], electrochromic [28], anticancer [29], and gas sensing [30]. WO_3 is an n-type semiconductor with a large band gap (around 2.7–3.5 eV) and is non-toxic. One of the most important characteristics of WO_3 is its morphological assortment. It can be designed in different dimensional morphologies, such as nanoparticles [31], nanowires [32], nanofibers [33], nanorods [31], nanosheets [34], and nanoplates [35]. It is shown that some special morphologies of WO_3 nanostructures are more appropriate for particular applications. With the emergence of nanotechnology as a progressive branch of science in recent years, the radiation protection system has also used various types of nanoparticles [36–38]. The fundamental supposition of the investigations

was that the application of nanoparticles leads to a more even distribution within the matrix compared to particles with micrometric size, and, hence, a better attenuation will be attained. Dong Yu found that the γ attenuation of nano-sized WO_3 was greater than the micro-sized particles [39]. Tekin et al. showed that the materials doped with nano-sized WO_3 displayed better shielding characteristics than materials doped with micro-sized WO_3 particles [37]. Kazemi et al. demonstrated, using the MCNPX model, that composites with WO_3 nanoparticles had mass attenuation coefficients greater than those of composites with WO_3 microparticles [40].

To the best of our knowledge, there is no study regarding the effect of WO_3 nanoparticles on the radiation-shielding characteristics of ceramic materials. Thus, we aim in this work to study, for the first time, the radiation attenuation of STO ceramic mixed with WO_3 nanoparticles. Different radiation shielding parameters were experimentally measured and discussed.

2. Experimental Procedure

2.1. Synthesis of Materials

All chemicals, strontium carbonate ($SrCO_3$), titanium dioxide (TiO_2), and tungsten trioxide nanoparticles (WO_3 NPs), were reagent grade and used without further purification. First, stoichiometric strontium titanate $SrTiO_3$ (STO for brevity) was synthesized using the solid-state reaction by mixing finely in ball milling media $SrCO_3$ and TiO_2 powders. The obtained mixture was sintered at 1300 °C for 5 h to form $SrTiO_3$ ceramic (STO for brevity), as shown in Equation (1).

$$SrCO_3 + TiO_2 \Rightarrow SrTiO_3 + CO_2 \quad (1)$$

In the second stage, different amounts of WO_3 NPs (x = 0, 2, 5, and 10 wt.%) were added to the STO sample. The mixtures were then compacted into pellets using PVA, which plays the role of the binder. The resulting pellets were placed in crucible alumina, then sintered at 1500° to obtain compact and dense ceramics of pristine STO ceramic (x = 0 wt.%) and WO_3-doped STO ceramics (x = 2, 5, and 10 wt.%). Then, the obtained ceramic samples were given for various characterizations.

2.2. Characterization of Ceramics

The crystallinity and phase analysis of the prepared ceramics were analyzed using a Rigaku Benchtop Miniflex powder XRD instrument with Cu Kα radiation. Using the Bruker alpha-II FT-IR spectrometer, the FT-IR spectra were recorded in the region of 400–4000 cm^{-1}. The γ-ray shielding parameters of STO-WO_3 NPs ceramics, such as linear attenuation coefficient (LAC), were experimentally determined using a high pure germanium (HPGe) detector and different point sources (Co-60, Cs-137, and Am-241). Readings resulting from the detector were processed using the Genie 2000 program. This program displays the intensity (count rate) for each photon that fell on the detector and was discovered during the measured time. From this point, the intensity of each specific energy was measured in the presence (I) and the absence (I_0) of the absorption sample. Then, by knowing the thickness of the absorption sample (t), the following law is used to calculate the LAC, which represents the possibility of the photon interaction through a certain distance within the absorption sample [41].

$$I = I_0\, e^{-LAC\,.\,t} \qquad \text{then,} \qquad LAC = \frac{1}{t}\ln\frac{I_0}{I} \quad (2)$$

The other attenuation factors-based LAC determination, such as half and tenth value layers (HVL, TVL) and radiation absorption factor (RAP). The definition and laws of these factors were reported in previously published papers [42,43].

3. Results and Discussion

3.1. Structural and Functional Analysis

The synthesized ceramics were analyzed using XRD and FT-IR to investigate the structural and compositional properties. Figure 1 depicts the XRD patterns of $SrTiO_3$ (STO) doped with different amounts of WO_3 NPs. Pure STO exhibits (100), (110), (111), (200), (210), (211), (220), and (310) planes corresponding to cubic perovskite structure (space group: Pm-3 m) of $SrTiO_3$ which are in agreement with JCPDS card no. 35–0734. The ceramic doped with x = 2 wt.% of WO_3 NPs does not contain any impurity. However, the secondary phase of $SrWO_4$ (marked as '*' in the figure; card no. 85–0587) appeared for x = 5 and 10% of WO_3 NPs, indicating that WO_3 NPs may react with the host material (STO) during the sintering process. The peak intensity of the impurity phase increases remarkably as the content of WO_3 NPs increases. The structural parameters, such as crystal cell parameter 'a' as well as the unit cell volume 'V' for all as-prepared ceramics calculated from the XRD data, are listed in Table 1. It is evident that the structural parameters 'a' and V' are higher for doped samples compared to the STO pristine sample. This effect can be attributed to the difference in ionic radii between the W element (0.66 Å) derived from WO_3 NPs dopant and Ti element (0.605 Å) derived from the host $SrTiO_3$. The presence of the $SrWO_4$ secondary phase can also be another reason for the lattice expansion in WO_3-doped STO ceramics.

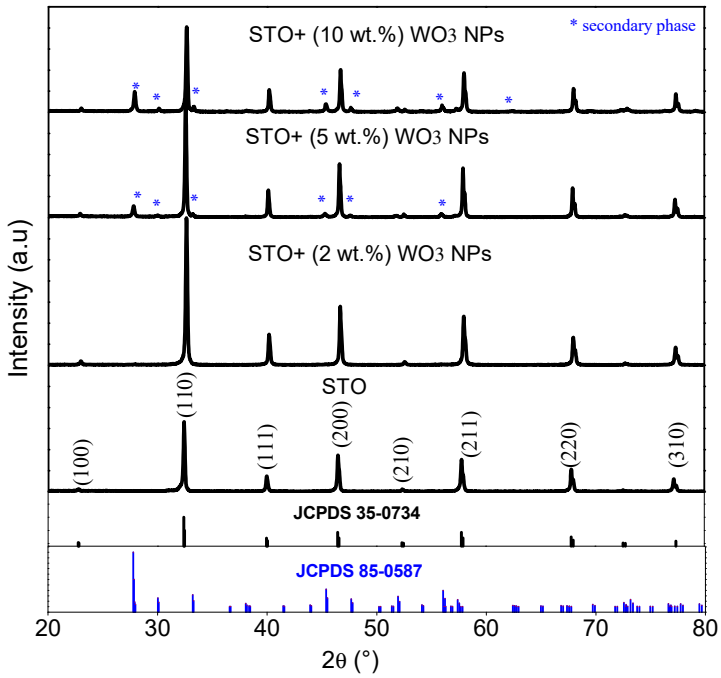

Figure 1. XRD patterns of STO ceramic and STO ceramics doped with *x* wt.% of WO_3 NPs.

Table 1. Structural parameters deduced from XRD analysis.

Ceramics	STO	STO + (2%) WO_3 NPs	STO + (5%) WO_3 NPs	STO + (10%) WO_3 NPs
a (Å)=	3.9020	3.9047	3.9032	3.9042
V ($Å^3$)=	59.4103	59.5337	59.4651	59.5108
Structure	Cubic	Cubic	Cubic	Cubic
d_{XRD} (nm)=	45.48	41.17	45.49	50.86

The crystallites size (d_{XRD}) is estimated for all ceramics by using the Scherrer equation [44]:

$$d_{XRD} = \frac{k\,\lambda}{\beta\,\cos\theta} \quad (3)$$

where k is a constant close to unity (k = 0.9), β is full width at half maximum, and θ is Bragg's angle. The calculated d_{XRD} values for various ceramics are registered in Table 1 and are found to be in the range of 50.86–41.17 nm. Compared to the pristine sample, the crystallite size first reduces for the sample doped with a low amount of WO_3, suggesting that WO3 NPs act as inhibitors for the grain growth of STO ceramic [45]. With further increasing the amount of WO_3, the d_{XRD} return to increase. This unexpected result may be due to the transformation of tungsten oxide into metal tungstate. Indeed, for high amounts of WO_3, a new second phase of $SrWO_4$ was detected, which is mainly attributed to the possible reaction between the host STO phase and WO_3 NPs. It can be then assumed that the newly formed phase may result in initiating the growth process of aggregate particles by coalescence [46]. Further analysis is needed to validate this assumption, which will be the aim of our future work.

The functional groups of all ceramics were characterized using FTIR analysis, as depicted in Figure 2. In the measured range, several distinct absorption bands were detected for the pristine STO ceramic. The signal at about 560 cm^{-1} is related to the characteristic stretching vibration of the Sr-Ti-O bond [47], which confirms the successful formation of the $SrTiO_3$ phase. This peak is maintained in the FTIR spectra of doped ceramics, confirming that the STO host perovskite structure is preserved. Another characteristic band with small intensity is observed around 1100 cm^{-1}, which can be attributed to the C=O stretching modes [48]. A large band around 3000 cm^{-1} is also observed for STO ceramic, which may be assigned to the O–H stretching modes [49]. Additional bands around 825 cm^{-1} appeared for ceramics doped with x = 5 and 10% of WO_3 NPs. This band is most probably a result of the signals of the W-O stretching vibration [50].

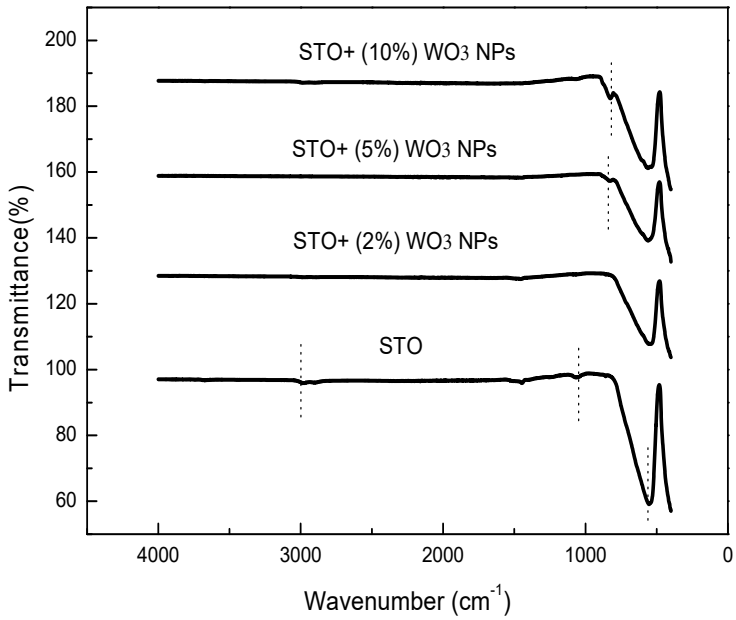

Figure 2. FT-IR results of STO ceramic and STO ceramic doped with x% of WO_3 NPs.

3.2. Radiation Attenuation Analysis

Figure 3 demonstrates the MAC (mass attenuation coefficient) of the prepared samples at four tested energies. At the first energy, the MAC values increase as more WO_3 nanoparticles are added to the ceramic. For example, the MAC of the WO_3-free ceramic is equal to 1.821 cm^{-1} at this energy, while the MAC of the ceramic with 10% WO_3 nanoparticles is equal to 2.188 cm^{-1}. From MAC determination and the density of ceramic samples, the LACs (linear attenuation coefficients) of the prepared ceramic samples can be calculated. Figure 4 demonstrates the LACs of the prepared ceramic samples at four tested energies. At the first energy, the LAC values increase as more WO_3 nanoparticles are added to the ceramic. For example, the LAC of the WO_3-free ceramic is equal to 9.308 cm^{-1} at this

energy, while the LAC of the ceramic with 10% WO_3 nanoparticles is equal to 11.563 cm^{-1}. The same trend can be observed at higher energies, however, with a smaller difference. Nevertheless, these results show how the amount of WO_3 in the ceramics correlates with an improvement in their shielding abilities. In addition, this figure also shows that LACs have an inverse relationship with energy. More specifically, the STO ceramic with 2% WO_3 has an LAC equal to 9.810, 0.394, 0.288, and 0.270 cm^{-1} at 0.060, 0.662, 1.173, and 1.333 MeV, respectively. Thus, ceramics are most effective against low-energy photons.

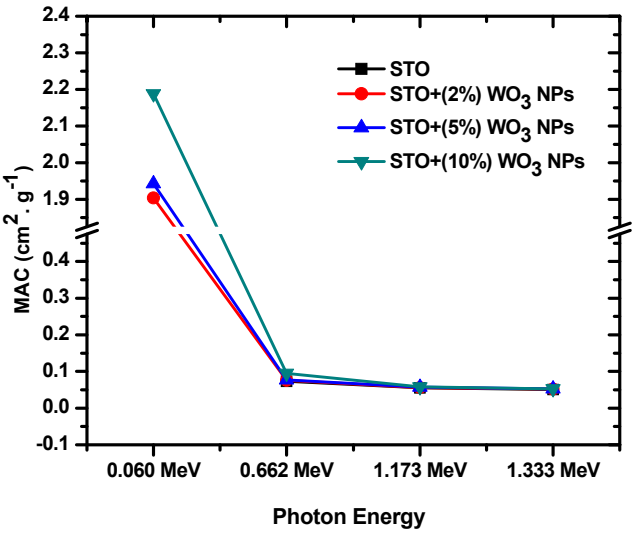

Figure 3. Mass attenuation coefficients of the STO ceramic and STO ceramic doped with x% of WO_3 NPs.

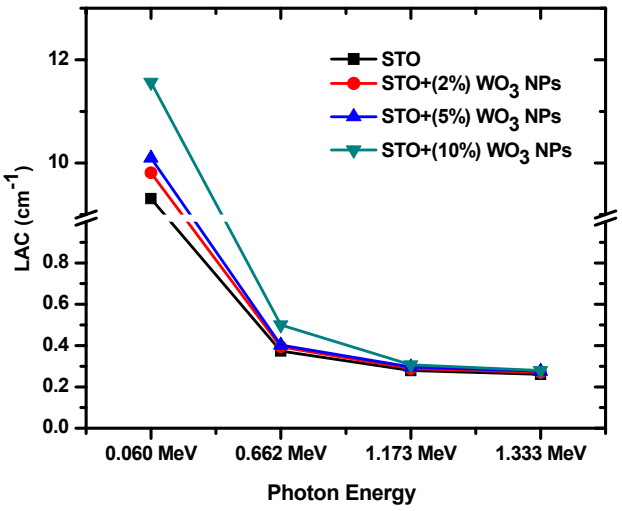

Figure 4. Linear attenuation coefficients of the STO ceramic and STO ceramic doped with x% of WO_3 NPs.

The half-value layer (HVL) of the investigated samples is graphed in Figure 5 against energy. For all the tested ceramics, their HVL values correlate with energy. For example, for the ceramic with 2% WO_3 nanoparticles, its HVL values are equal to 0.071 cm, 1.760 cm, 2.407 cm, and 2.564 cm at 0.060 MeV, 0.662 MeV, 1.173 MeV, and 1.333 MeV, respectively. As the energy increases, more radiation can pass through the material, which is why this relationship occurs. Therefore, a larger thickness is required to absorb half of the total photons, leading to a greater HVL. The figure also shows that HVL decreases with increasing WO_3 content. This trend is most evident at higher energies, such as 1.173 MeV. Moreover, at 1.173 MeV, the WO_3 values are equal to 2.483, 2.407, 2.334, and 2.259 cm for the samples with 0, 2, 5, and 10% WO_3 nanoparticles. Thus, increasing the amount of WO_3 nanoparticles in the ceramics improves their HVL values, lowering how thick a material needs to be to attenuate the same number of photons.

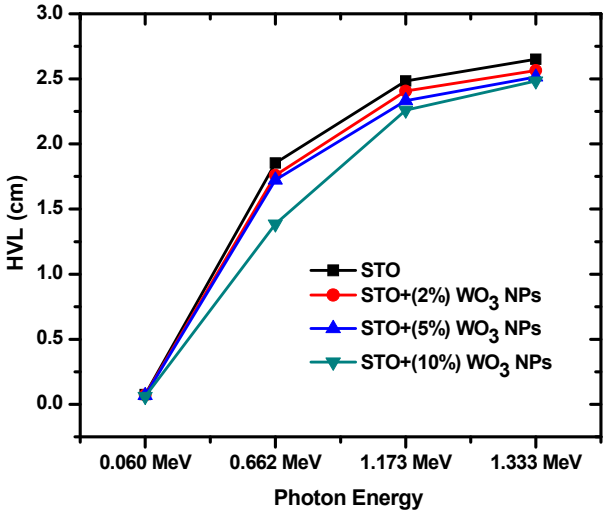

Figure 5. Half value layer of STO ceramic and STO ceramic doped with x% of WO_3 NPs.

The tenth value layer (TVL) is like HVL, except it is defined as how thick a material needs to be to absorb nine-tenths of the incoming photons. Because of this, similar trends can be observed between the two figures; however, all the TVL values are higher than their HVL counterpart. The same two trends can be observed in Figure 6. Mainly, the TVL values increase with energy. For example, the TVL values for the STO with no WO_3 nanoparticles are equal to 0.247, 6.158, 8.250, and 8.809 cm at 0.060, 0.662, 1.173, and 1.333 MeV, respectively. The second trend involves the relationship between TVL and photon energy. At 0.662 MeV, the STO ceramics have TVL values of 6.158, 5.848, 5.724, and 4.604 cm for the samples with 0, 2, 5, and 10% WO_3 nanoparticles. Thus, increasing the WO_3 content in the STO ceramics improves their shielding efficiency.

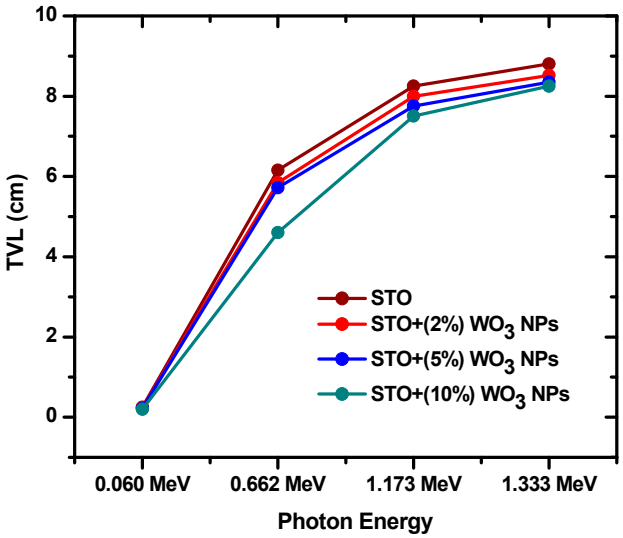

Figure 6. Tenth value layer of STO ceramic and STO ceramic doped with x% of WO_3 NPs.

The mean free path (MFP) of the STO ceramics is shown in Figure 7 at the four tested energies. The maximum MFP values occur for the STO ceramic, while the ceramic with 10% WO_3 nanoparticles has the minimum MFP values. For example, at 0.060 MeV, the STO ceramic has an MFP value of 0.107 cm, while the ceramic with 10% WO_3 NP has an MFP value of 0.086 cm. Thus, the amount of WO_3 in the ceramic mixture correlates with more collisions occurring within the sample, leading to greater attenuation. Furthermore, for any single ceramic, its MFP values increase with energy. For instance, STO-5WO_3's is equal to 0.099 cm, 2.486 cm, 3.367 cm, and 3.628 cm at 0.060, 0.662, 1.173, and 1.333 MeV.

Higher energy radiation tends to pass through the samples more easily, decreasing the number of collisions and increasing the distance between collisions. Thus, ceramics are able to attenuate lower energy photons than higher energy ones. The results of LAC, HVL, and MFP, as well as the mass attenuation coefficient (MAC), are reported in Table 2.

Table 2. The experimental values of the attenuator parameters for STO-ceramic samples.

Code	Energy (MeV)	STO	STO + 2% WO_3 NPs	STO + 5% WO_3 NPs	STO + 10% WO_3 NPs
LAC, cm^{-1}	0.060	9.308	9.810	10.097	11.563
	0.662	0.374	0.394	0.402	0.500
	1.173	0.279	0.288	0.297	0.307
	1.333	0.261	0.270	0.276	0.279
HVL, cm	0.060	0.074	0.071	0.069	0.060
	0.662	1.854	1.760	1.723	1.386
	1.173	2.483	2.407	2.334	2.259
	1.333	2.652	2.564	2.515	2.484
TVL, cm	0.060	0.247	0.235	0.228	0.199
	0.662	6.158	5.848	5.724	4.604
	1.173	8.250	7.997	7.753	7.505
	1.333	8.809	8.517	8.353	8.253
MAC, $cm^2 \cdot g^{-1}$	0.060	1.821	1.904	1.943	2.188
	0.662	0.073	0.076	0.077	0.095
	1.173	0.055	0.056	0.057	0.058
	1.333	0.051	0.052	0.053	0.053

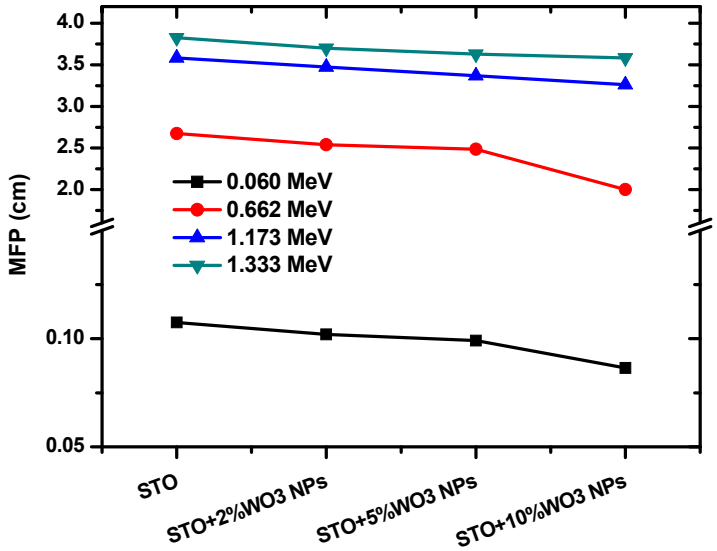

Figure 7. Mean free path of STO ceramic and STO ceramic doped with x% of WO_3 NPs.

The radiation protection efficiency (RPE) of the four prepared STO ceramics was calculated and graphed in Figure 8 at a thickness of 0.5 cm. RPE increases with WO_3 content at all tested energies. For instance, at 1.333 MeV, the RPE values are 12.25%, 12.64%, 12.87%, and 13.02% for the samples with 0, 2, 5, and 10% WO_3 nanoparticles. A greater RPE indicates a more effective shielding capability, so raising the amount of WO_3 in the ceramics leads to greater attenuation. Furthermore, RPE decreases as the energy of the incoming

photons increases. The RPE of the sample with no WO_3 is equal to 99.05 at 0.060 MeV and drops to 12.25% at 1.333 MeV. Meanwhile, the RPE of the sample with 10% of WO_3 nanoparticles is equal to 99.69% and 13.02% at 0.060 MeV and 1.333 MeV, respectively. This conclusion reinforces some of the results from the previous figures that more photons can be attenuated at lower energies.

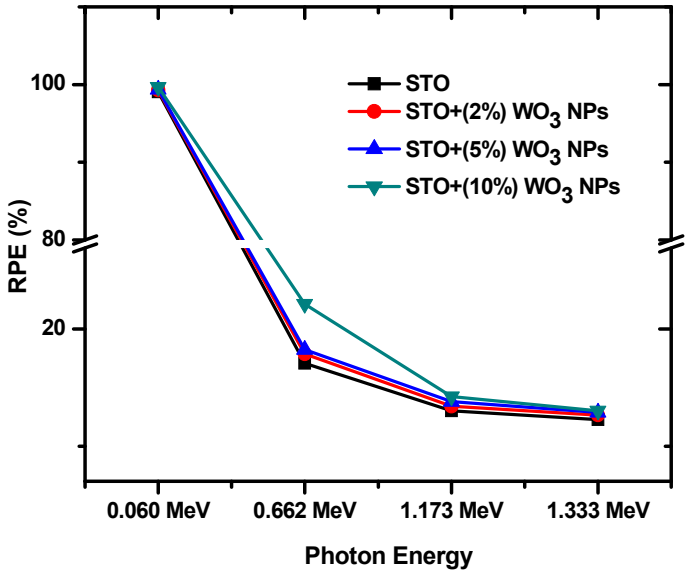

Figure 8. Radiation protection efficiency of STO ceramic and STO ceramic doped with x% of WO_3 NPs.

To compare the shielding abilities of the prepared ceramics with other radiation shields, Figure 9 graphs the LACs of the STO and STO + 10% of WO_3 NPs ceramics alongside four other shielding materials at 0.662 MeV. The STO and STO + 10% of WO_3 NPs ceramics had a greater LAC value than granite and marble [51,52]. SnTe and PbTe shields have a greater LAC than the STO ceramic but less than the STO + 10% of WO_3 ceramic [53]. Thus, ceramics have an overall very desirable shielding ability compared to other commonly used materials for radiation shielding purposes.

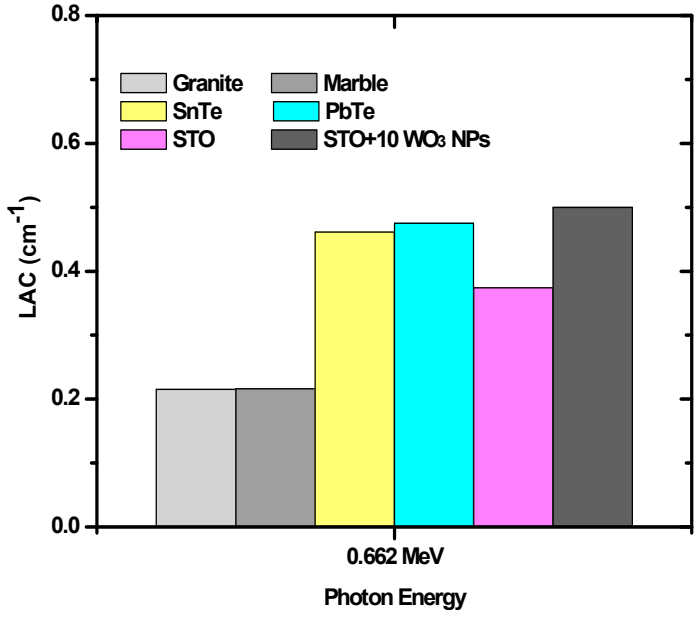

Figure 9. Linear attenuation coefficient for STO and STO + 10% WO_3 NPs ceramics alongside four other shielding materials at 0.662 MeV.

4. Conclusions

In this work, we proposed a strategy for developing new ceramic materials consisting of STO doped with WO_3 nanoparticles for the purpose of radiation protection. The different samples were prepared using the simple solid-state reaction method. The successful formation of the required compositions was confirmed by XRD and FTIR analyses. All as-prepared ceramics crystallized into the cubic structure. A new phase belonging to $SrWO_4$ was detected for 5 and 10% doped ceramics suggesting an interaction between the host STO and the dopant WO_3 NPs has occurred. The lattice constant 'a' and the unit cell volume 'V' were found to be higher for doped ceramic compared to the STO pristine ceramic. The crystallite size varied with the content of WO_3 NPs. In the second part, we focused on the role of adding WO_3 NPs in improving the radiation-protective characteristics of STO ceramics. The LAC was experimentally measured using a high pure germanium (HPGe) detector and three-point sources (^{60}C, ^{241}Am, and ^{137}Cs). The LAC of the WO_3-free ceramic at 0.06 MeV is equal to 9.308 cm^{-1}, while it is 11.563 cm^{-1} for the ceramic with 10% WO_3 nanoparticles. This shows that the LAC values increase as more WO_3 nanoparticles are added to the ceramic. We investigated the relationship between the LAC and the energy, and we concluded that the ceramics are most effective against low-energy photons. In order to examine the thickness of the ceramics that required attenuating certain levels of the photons, we evaluated the HVL and TVL. From the findings of both factors, we found that a larger thickness is required to absorb the photons with higher energies. Moreover, we examined the impact of WO_3 nanoparticles on these two factors. In brief, increasing the amount of WO_3 nanoparticles in the ceramics improves their HVL and TVL values. In addition to these factors, the MFP results also proved that the ceramics are able to attenuate lower energy photons than higher energy ones. At 1.333 MeV, the RPE for the samples with 0, 2, 5, and 10% WO_3 nanoparticles are 12.25%, 12.64%, 12.87%, and 13.02%, respectively. Hence, from the RPE data, we found that increasing the amount of WO_3 in the ceramics leads to greater attenuation.

Author Contributions: Conceptualization, M.E.; Data curation, M.I.S..; Funding acquisition, M.I.S. and S.H..; Investigation, M.I.S.; Methodology, M.E.; Project administration, S.H.; Resources, Y.S. and E.H.; Software, M.I.S.; Supervision, S.H.; Validation, Y.S.; Writing—original draft, Y.S. and E.H.; Writing—review and editing, Y.S. and E.H. All authors have read and agreed to the published version of the manuscript.

Funding: M.I. Sayyed and S. Hashim gratefully acknowledge Universiti Teknologi Malaysia for supporting their Prominent Visiting Researcher Scheme (RJ3000.7113.3F000) through the Department of Deputy Vice-Chancellor (Research and Innovation).

Institutional Review Board Statement: Not applicable.

Informed Consent Statement: Not applicable.

Data Availability Statement: All relevant data are within this paper.

Acknowledgments: M.I. Sayyed and S. Hashim gratefully acknowledge Universiti Teknologi Malaysia for providing Prominent Visiting Researcher Scheme (RJ3000.7113.3F000) by the Department Deputy of Vice-Chancellor (Research and Innovation).

Conflicts of Interest: The authors declare no conflict of interest.

References

1. Shultis, J.K.; Faw, R.E. Radiation shielding technology. *Health Phys.* **2005**, *88*, 297–322. [CrossRef] [PubMed]
2. Amana, M.S.; Aldhuhaibat, M.J.R.; Salim, A.A. Evaluation of the absorption, scattering and overall probability of gamma rays in lead and concrete interactions. *SCIOL Biomed.* **2021**, *4*, 191–199.
3. Hassan, H.E.; Badran, H.M.; Aydarous, A.; Sharshar, T. Studying the effect of nano lead compounds additives on the concrete shielding properties for γ-rays. *Nucl. Instrum. Methods Phys. Res. Sect. B Beam Interact. Mater. At.* **2015**, *360*, 81–89. [CrossRef]
4. Hannachi, E.; Sayyed, M.I.; Slimani, Y.; Almessiere, M.A.; Baykal, A.; Elsafi, M. Synthesis, characterization, and performance assessment of new composite ceramics towards radiation shielding applications. *J. Alloys Compd.* **2022**, *899*, 163173. [CrossRef]

5. Sayyed, M.I.; Hannachi, E.; Mahmoud, K.A.; Slimani, Y. Synthesis of different (RE) BaCuO ceramics, study their structural properties, and tracking their radiation protection efficiency using Monte Carlo simulation. *Mater. Chem. Phys.* **2022**, *276*, 125412. [CrossRef]
6. Sayyed, M.I.; El-Mesady, I.A.; Abouhaswa, A.S.; Askin, A.; Rammah, Y.S. Comprehensive study on the structural, optical, physical and gamma photon shielding features of B2O3-Bi2O3-PbO-TiO2 glasses using WinXCOM and Geant4 code. *J. Mol. Struct.* **2019**, *1197*, 656–665. [CrossRef]
7. Aygün, B.; Şakar, E.; Agar, O.; Sayyed, M.I.; Karabulut, A.; Singh, V.P. Development of new heavy concretes containing chrome-ore for nuclear radiation shielding applications. *Prog. Nucl. Energy* **2021**, *133*, 103645. [CrossRef]
8. Khazaalah, T.H.; Shahrim Mustafa, I.; Al-Ghamdi, H.; Abdul Rahman, A.; Sayyed, M.I.; Almuqrin, A.H.; Mohd Zaid, M.H.; Hisam, R.; Abdul Malik, M.F.I.; Seth Ezra, N.; et al. The Effect of WO_3-Doped Soda Lime Silica SLS Waste Glass to Develop Lead-Free Glass as a Shielding Material against Radiation. *Sustainability* **2022**, *14*, 2413. [CrossRef]
9. Sayyed, M.I.; Hamad, M.K.; Mhareb, M.H.A.; Kurtulus, R.; Dwaikat, N.; Saleh, M.; Elsafi, M.; Taki, M.M.; Kavas, T.; Ziq, K.A.; et al. Assessment of radiation attenuation properties for novel alloys: An experimental approach. *Radiat. Phys. Chem.* **2022**, *200*, 110152. [CrossRef]
10. Bagheri, R.; Shirmardi, S.P. Gamma-ray shielding studies on borate glasses containing BaO, Bi_2O_3, and PbO in different concentrations. *Radiat. Phys. Chem.* **2021**, *184*, 109434. [CrossRef]
11. Bagheri, R.; Adeli, R. Gamma-ray shielding properties of phosphate glasses containing Bi_2O_3, PbO, and BaO in different rates. *Radiat. Phys. Chem.* **2020**, *174*, 108918. [CrossRef]
12. Kavaz, E.; El_Agawany, F.I.; Tekin, H.O.; Perişanoğlu, U.; Rammah, Y.S. Nuclear radiation shielding using barium borosilicate glass ceramics. *J. Phys. Chem. Solids* **2020**, *142*, 109437. [CrossRef]
13. Bagheri, R.; Moghaddam, A.K.; Shirmardi, S.P.; Azadbakht, B.; Salehi, M. Determination of gamma-ray shielding properties for silicate glasses containing $Bi2O_3$, PbO, and BaO. *J. Non-Cryst. Solids* **2018**, *479*, 62–71. [CrossRef]
14. Bagheri, R.; Moghaddam, A.K.; Yousefnia, H. Gamma ray shielding study of barium–bismuth–borosilicate glasses as transparent shielding materials using MCNP-4C code, XCOM program, and available experimental data. *Nucl. Eng. Technol.* **2017**, *49*, 216–223. [CrossRef]
15. Slimani, Y.; Unal, B.; Almessiere, M.A.; Hannachi, E.; Yasin, G.; Baykal, A.; Ercan, I. Role of WO_3 nanoparticles in electrical and dielectric properties of $BaTiO_3$–$SrTiO_3$ ceramics. *J. Mater. Sci. Mater. Electron.* **2020**, *31*, 7786–7797. [CrossRef]
16. Shi, X.L.; Wu, H.; Liu, Q.; Zhou, W.; Lu, S.; Shao, Z.; Dargusch, M.; Chen, Z.G. $SrTiO_3$-based thermoelectrics: Progress and challenges. *Nano Energy* **2020**, *78*, 105195. [CrossRef]
17. Slimani, Y.; Selmi, A.; Hannachi, E.; Almessiere, M.A.; Baykal, A.; Ercan, I. Impact of ZnO addition on structural, morphological, optical, dielectric and electrical performances of $BaTiO_3$ ceramics. *J. Mater. Sci. Mater. Electron.* **2019**, *30*, 9520–9530. [CrossRef]
18. Abbas, M.I.; El-Khatib, A.M.; Dib, M.F.; Mustafa, H.E.; Sayyed, M.I.; Elsafi, M. The Influence of Bi2O3 Nanoparticle Content on the γ-ray Interaction Parameters of Silicon Rubber. *Polymers* **2022**, *14*, 1048. [CrossRef]
19. Enzlberger, L. Photovoltaic Properties of SrTiO3-δ in Single Crystalline and Thin Film cells. Ph.D. Thesis, Technische Universität Wien, Vienna, Austria, 2022.
20. Aravinthkumar, K.; Praveen, E.; Mary, A.J.R.; Mohan, C.R. Investigation on $SrTiO_3$ nanoparticles as a photocatalyst for enhanced photocatalytic activity and photovoltaic applications. *Inorg. Chem. Commun.* **2022**, *140*, 109451. [CrossRef]
21. Wang, J.; Wang, T.; Zhao, Z.; Wang, R.; Wang, C.; Zhou, F.; Li, S.; Zhao, L.; Feng, M. Regulation of oxygen vacancies in $SrTiO_3$ perovskite for efficient photocatalytic nitrogen fixation. *J. Alloys Compd.* **2022**, *902*, 163865. [CrossRef]
22. Liu, L.; Chu, B.; Li, P.; Fu, P.; Du, J.; Hao, J.; Li, W.; Zeng, H. Achieving high energy storage performance and ultrafast discharge speed in $SrTiO_3$-based ceramics via a synergistic effect of chemical modification and defect chemistry. *Chem. Eng. J.* **2022**, *429*, 132548. [CrossRef]
23. Hannachi, E.; Sayyed, M.I.; Albarzan, B.; Almuqrin, A.H.; Mahmoud, K.A. Synthesis and study of structural, optical and radiation-protective peculiarities of $MTiO_3$ (M = Ba, Sr) metatitanate ceramics mixed with SnO_2 oxide. *Ceram. Int.* **2021**, *47*, 28528–28535. [CrossRef]
24. Slimani, Y.; Hamad, M.K.; Olarinoye, I.O.; Alajerami, Y.S.; Sayyed, M.I.; Almessiere, M.A.; Mhareb, M.H.A. Determination of structural features of different Perovskite ceramics and investigation of ionizing radiation shielding properties. *J. Mater. Sci. Mater. Electron.* **2021**, *32*, 20867–20881. [CrossRef]
25. Hannachi, E.; Sayyed, M.I.; Mahmoud, K.A.; Slimani, Y.; Akhtar, S.; Albarzan, B.; Almuqrin, A.H. Impact of tin oxide on the structural features and radiation shielding response of some ABO3 perovskites ceramics (A = Ca, Sr, Ba; B = Ti). *Appl. Phys. A* **2021**, *127*, 1–12. [CrossRef]
26. Pehlivan, I.B.; Atak, G.; Niklasson, G.A.; Stolt, L.; Edoff, M.; Edvinsson, T. Electrochromic solar water splitting using a cathodic WO_3 electrocatalyst. *Nano Energy* **2021**, *81*, 105620. [CrossRef]
27. Dutta, V.; Sharma, S.; Raizada, P.; Thakur, V.K.; Khan, A.A.P.; Saini, V.; Asiri, A.M.; Singh, P. An overview on WO_3 based photocatalyst for environmental remediation. *J. Environ. Chem. Eng.* **2021**, *9*, 105018. [CrossRef]
28. Chang, C.M.; Chiang, Y.C.; Cheng, M.H.; Lin, S.H.; Jian, W.B.; Chen, J.T.; Cheng, Y.J.; Ma, Y.R.; Tsukagoshi, K. Fabrication of WO_3 electrochromic devices using electro-exploding wire techniques and spray coating. *Sol. Energy Mater. Sol. Cells* **2021**, *223*, 110960. [CrossRef]

29. Qureshi, N.; Lee, S.; Chaudhari, R.; Mane, P.; Pawar, J.; Chaudhari, B.; Shinde, M.; Rane, S.; Kim, T.; Amalnerkar, D. Hydrothermal Generation of 3-Dimensional WO3 Nanocubes, Nanobars and Nanobricks, Their Antimicrobial and Anticancer Properties. *J. Nanosci. Nanotechnol.* **2021**, *21*, 5337–5343. [CrossRef]
30. Du, Q.; Wang, L.; Yang, J.; Liu, J.; Yuan, Y.; Wang, M.; Liu, B.; Zhang, X.; Ren, Y.; Zhao, H.; et al. Enhancing gas sensing performances and sensing mechanism at atomic and molecule level of WO3 nanoparticles by hydrogenation. *Sens. Actuators B Chem.* **2018**, *273*, 1786–1793. [CrossRef]
31. Hemily, H.M.; Saleh, I.H.; Ghataas, Z.F.; Abdel-Halim, A.A.; Hisam, R.; Shah, A.Z.; Sayyed, M.I.; Yasmin, S.; Elsafi, M. Radiation Shielding Enhancement of Polyester Adding Artificial Marble Materials and WO3 Nanoparticles. *Sustainability* **2022**, *14*, 13355. [CrossRef]
32. Zeb, S.; Sun, G.; Nie, Y.; Cui, Y.; Jiang, X. Synthesis of highly oriented WO_3 nanowire bundles decorated with Au for gas sensing application. *Sens. Actuators B Chem.* **2020**, *321*, 128439. [CrossRef]
33. Xiao, Y.; He, Z.; Wang, R.; Tao, X.; Li, B. Synthesis of WO_3 nanofibers decorated with BiOCl nanosheets for photocatalytic degradation of organic pollutants under visible light. *Colloids Surf. A Physicochem. Eng. Asp.* **2019**, *580*, 123752. [CrossRef]
34. Lei, J.; Liu, H.; Yuan, C.; Chen, Q.; Liu, J.A.; Wen, F.; Jiang, X.; Deng, W.; Cui, X.; Duan, T.; et al. Enhanced photoreduction of U (VI) on WO3 nanosheets by oxygen defect engineering. *Chem. Eng. J.* **2021**, *416*, 129164. [CrossRef]
35. Kong, L.; Guo, X.; Xu, J.; Mo, Z.; Li, L. Morphology control of WO_3 nanoplate film on W foil by oxalic acid for photocatalytic gaseous acetaldehyde degradation. *J. Photochem. Photobiol. A Chem.* **2020**, *401*, 112760. [CrossRef]
36. Ghavami, S.M.; Ghiasi, H.; Mesbahi, A. Monte Carlo modeling of the yttrium-90 nanospheres application in the liver radionuclide therapy and organs doses calculation. *Nucl. Technol. Radiat. Prot.* **2016**, *31*, 89–96. [CrossRef]
37. Tekin, H.O.; Singh, V.P.; Manici, T. Effects of micro-sized and nano-sized WO3 on mass attenauation coefficients of concrete by using MCNPX code. *Appl. Radiat. Isot.* **2017**, *121*, 122–125. [CrossRef] [PubMed]
38. Mesbahi, A.; Famouri, F.; Ahar, M.J.; Ghaffari, M.O.; Ghavami, S.M. A study on the imaging characteristics of Gold nanoparticles as a contrast agent in X-ray computed tomography. *Pol. J. Med. Phys. Eng.* **2017**, *23*, 9. [CrossRef]
39. Al-Ghamdi, H.; Hemily, H.M.; Saleh, I.H.; Ghataas, Z.F.; Abdel-Halim, A.A.; Sayyed, M.I.; Yasmin, S.; Almuqrin, A.H.; Elsafi, M. Impact of WO3-Nanoparticles on Silicone Rubber for Radiation Protection Efficiency. *Materials* **2022**, *15*, 5706. [CrossRef]
40. Elsafi, M.; Dib, M.F.; Mustafa, H.E.; Sayyed, M.I.; Khandaker, M.U.; Alsubaie, A.; Almalki, A.S.A.; Abbas, M.I.; El-Khatib, A.M. Enhancement of Ceramics Based Red-Clay by Bulk and Nano Metal Oxides for Photon Shielding Features. *Materials* **2021**, *14*, 7878. [CrossRef]
41. El-Khatib, A.M.; Elsafi, M.; Almutiri, M.N.; Mahmoud, R.M.M.; Alzahrani, J.S.; Sayyed, M.I.; Abbas, M.I. Enhancement of Bentonite Materials with Cement for Gamma-Ray Shielding Capability. *Materials* **2021**, *14*, 4697. [CrossRef]
42. Hannachi, E.; Sayyed, M.I.; Slimani, Y.; Elsafi, M. Experimental investigation on the physical properties and radiation shielding efficiency of YBa2Cu3Oy/M@ M3O4 (M = Co, Mn) ceramic composites. *J. Alloys Compd.* **2022**, *904*, 164056. [CrossRef]
43. Al-Hadeethi, Y.; Sayyed, M.I.; Barasheed, A.Z.; Ahmed, M.; Elsafi, M. Fabrication of lead free borate glasses modified by bismuth oxide for gamma ray protection applications. *Materials* **2022**, *15*, 789. [CrossRef]
44. Hannachi, E.; Almessiere, M.A.; Slimani, Y.; Baykal, A.; Azzouz, F.B. AC susceptibility investigation of YBCO superconductor added by carbon nanotubes. *J. Alloys Compd.* **2020**, *812*, 152150. [CrossRef]
45. Hikichi, Y.; Niimi, T.; Sato, H. Preparation and Dielectric Properties of WO3-Doped Small-Grained $BaTiO_3$ Ceramics. *Jpn. J. Appl. Phys.* **1985**, *24*, 1039. [CrossRef]
46. Sczancoski, J.C.; Cavalcante, L.S.; Joya, M.R.; Espinosa, J.W.M.; Pizani, P.S.; Varela, J.A.; Longo, E. Synthesis, growth process and photoluminescence properties of $SrWO_4$ powders. *J. Colloid Interface Sci.* **2009**, *330*, 227–236. [CrossRef] [PubMed]
47. Hou, D.; Hu, X.; Ho, W.; Hu, P.; Huang, Y. Facile fabrication of porous Cr-doped $SrTiO_3$ nanotubes by electrospinning and their enhanced visible-light-driven photocatalytic properties. *J. Mater. Chem. A* **2015**, *3*, 3935–3943. [CrossRef]
48. Šetinc, T.; Spreitzer, M.; Vengust, D.; Jerman, I.; Suvorov, D. Inherent defects in sol-precipitation/hydrothermally derived SrTiO3 nanopowders. *Ceram. Int.* **2013**, *39*, 6727–6734. [CrossRef]
49. Adireddy, S.; Lin, C.; Cao, B.; Zhou, W.; Caruntu, G. Solution-based growth of monodisperse cube-like $BaTiO_3$ colloidal nanocrystals. *Chemi. Mater.* **2010**, *22*, 1946–1948. [CrossRef]
50. Adhikari, S.; Sarkar, D.; Maiti, H.S. Synthesis and characterization of WO3 spherical nanoparticles and nanorods. *Mater. Res. Bull.* **2014**, *49*, 325–330. [CrossRef]
51. Elsafi, M.; Alrashedi, M.F.; Sayyed, M.I.; Al-Hamarneh, I.F.; El-Nahal, M.A.; El-Khatib, M.; Khandaker, M.U.; Osman, H.; Askary, A.E. The Potentials of Egyptian and Indian Granites for Protection of Ionizing Radiation. *Materials* **2021**, *14*, 3928. [CrossRef]
52. Elsafi, M.; El-Nahal, M.A.; Alrashedi, M.F.; Olarinoye, O.I.; Sayyed, M.I.; Khandaker, M.U.; Osman, H.; Alamri, S.; Abbas, M.I. Shielding properties of some marble types: A comprehensive study of experimental and XCOM results. *Materials* **2021**, *14*, 4194. [CrossRef] [PubMed]
53. Mhareb, M.H.A.; Zeama, M.; Elsafi, M.; Alajerami, Y.S.; Sayyed, M.I.; Saleh, G.; Hamad, R.M.; Hamad, M.K. Radiation shielding features for various tellurium-based alloys: A comparative study. *J. Mater. Sci. Mater. Electron.* **2021**, *32*, 26798–26811. [CrossRef]